

# Spin-Degenerate Bulk Bands and Topological Surface States of $\text{RuO}_2$

T. Osumi,<sup>1</sup> K. Yamauchi,<sup>2</sup> S. Souma,<sup>3,4,\*</sup> P. Shubhankar,<sup>5,6</sup> A. Honma,<sup>1</sup> K. Nakayama,<sup>1</sup> K. Ozawa,<sup>7</sup> M. Kitamura,<sup>8</sup> K. Horiba,<sup>8</sup> H. Kumigashira,<sup>9</sup> C. Bigi,<sup>10</sup> F. Bertran,<sup>10</sup> T. Oguchi,<sup>2</sup> T. Takahashi,<sup>1</sup> Y. Maeno,<sup>5</sup> and T. Sato<sup>1,3,4,11,12,\*</sup>

<sup>1</sup>*Department of Physics, Graduate School of Science,  
Tohoku University, Sendai 980-8578, Japan*

<sup>2</sup>*Center for Spintronics Research Network (CSRN),  
Osaka University, Toyonaka, Osaka 560-8531, Japan*

<sup>3</sup>*Advanced Institute for Materials Research (WPI-AIMR),  
Tohoku University, Sendai 980-8577, Japan*

<sup>4</sup>*Center for Science and Innovation in Spintronics (CSIS),  
Tohoku University, Sendai 980-8577, Japan*

<sup>5</sup>*Toyota Riken-Kyoto University Research Center (TRiKUC), Kyoto 606-8501, Japan*

<sup>6</sup>*Indian Institute of Technology (IIT) Kanpur, Kanpur 208016, India*

<sup>7</sup>*Institute of Materials Structure Science,  
High Energy Accelerator Research Organization (KEK), Tsukuba, Ibaraki 305-0801, Japan*

<sup>8</sup>*National Institutes for Quantum Science and Technology (QST), Sendai 980-8579, Japan*

<sup>9</sup>*Institute of Multidisciplinary Research for Advanced Materials (IMRAM),  
Tohoku University, Sendai 980-8577, Japan*

<sup>10</sup>*Synchrotron SOLEIL, L'Orme des Merisiers,  
Départementale 128, 91190 Saint-Aubin, France*

<sup>11</sup>*International Center for Synchrotron Radiation Innovation Smart (SRIS),  
Tohoku University, Sendai 980-8577, Japan*

<sup>12</sup>*Mathematical Science Center for Co-creative Society (MathCCS),  
Tohoku University, Sendai 980-8577, Japan*

(Dated: January 22, 2025)

## Abstract

Altermagnets are a novel platform to realize exotic electromagnetic properties distinct from those of conventional ferromagnets and antiferromagnets. We report results of micro-focused angle-resolved photoemission spectroscopy (ARPES) on RuO<sub>2</sub>, of which altermagnetic nature has been under fierce debate. We have elucidated the band structure of the (100), (110) and (101) surfaces of a bulk single crystal. We found that, irrespective of the surface orientation, the experimental band structures obtained by ARPES commonly show a semi-quantitative agreement with the bulk-band calculation for the nonmagnetic phase, but display a severe disagreement with that for the antiferromagnetic phase. Moreover, spin-resolved ARPES signifies a negligible spin polarization for the bulk bands. These results suggest the absence of antiferromagnetism and altermagnetic spin splitting. Furthermore, we identified a flat surface band and a dispersive one near the Fermi level at the (100)/(110) and (101) surfaces, respectively, both of which are attributed to the topological surface states associated with the bulk Dirac nodal lines. The present ARPES results suggest that the crystal-orientation-dependent topological surface/interface states need to be taken into account to properly capture the transport and catalytic characteristics of RuO<sub>2</sub>.

---

\* Corresponding authors:

seigo.soma.e2@tohoku.ac.jp

t-sato@arpes.phys.tohoku.ac.jp

## I. INTRODUCTION

The coupling of spin and charge is one of key ingredients to give rise to novel quantum phases. When the space inversion symmetry is broken in materials such as noncentrosymmetric bulk crystals and heterostructures, the energy bands become spin split due to the spin-orbit coupling (SOC) [1, 2]. These spin-split bands exhibit a momentum-dependent spin texture (spin-momentum locking), leading to novel functionalities in spintronics such as spin-Hall effect and spin-charge conversion [3–6]. They are also responsible for various exotic physical properties such as unconventional superconductivity and superconducting diode effect [7–11]. Recent theoretical proposals together with the experimental verification of momentum-dependent spin splitting in some collinear antiferromagnets are revolutionizing the field of spintronics and spin-related physics, because the splitting can be realized even without SOC [12–20]. In these antiferromagnets called altermagnets [19, 20], the existence of opposite-spin sublattices connected by a certain symmetry of crystal triggers an anisotropic sign-changing spin splitting associated with the breaking of  $PT$  symmetry (combination of space-inversion and time-reversal symmetries). Intriguingly, the magnitude of splitting reaches as large as 1 eV, which is even larger than the SOC-induced spin splitting, making altermagnets an excellent platform to realize novel electromagnetic properties associated with the spin-charge coupling [13, 14, 16–20].

$\text{RuO}_2$  with rutile structure [see Fig. 1(a)] has attracted significant attention because of its outstanding properties associated with the spin-charge coupling [12, 15, 21, 22], provoking active discussions on whether these properties are attributable to the altermagnetic spin splitting [22–31]. In fact, the observed magnitude of the spin Hall effect is two orders of magnitude smaller than the expectation. When one assumes a collinear antiferromagnetic (AFM) structure [12, 32–34], the oxygen atoms surrounding the Ru atoms break the  $PT$  symmetry [Fig. 1(a)], resulting in a  $d$ -wave-like anisotropic spin splitting of maximally 0.8 eV along the [101] direction with gap nodes in the (100) and (010) planes [15, 22]. This anisotropic splitting was theoretically predicted to give rise to a giant anomalous Hall effect and highly efficient spin-charge conversion, both of which show a strong crystallographic-axis dependence [15, 21, 22]. These predictions have been examined experimentally using thin-film samples with various crystal orientations [22–25, 27–30], as highlighted by the observation of anomalous Hall conductivity comparable to that of Fe in a (110)-oriented sample [22] and high spin-charge conversion efficiency in a (101)-oriented sample [21, 25].

RuO<sub>2</sub> also shows intriguing physical and chemical properties such as anisotropic anomalous Nernst effect [35], anisotropic tunneling magnetoresistance [36, 37], terahertz emission [38, 39], and catalytic reactivity on the (110) surface [40], while their relationship with the electronic states has yet to be clarified.

While the experimental evidence showing the crystal-orientation-dependence to support the anisotropic spin splitting is accumulating in RuO<sub>2</sub> [22–24, 26–30], there exist some contradictory reports from the neutron scattering and  $\mu$ SR [41, 42] that do not support the magnetic order. Consequently, there remain two key unresolved questions; i.e. (i) whether RuO<sub>2</sub> truly exhibits altermagnetism, and (ii) what microscopic electronic structures underlie the observed strong crystal-orientation-dependent transport properties. Although angle-resolved photoemission spectroscopy (ARPES) is considered to be one of essential techniques for addressing these issues through direct observation of the band structure, current ARPES studies are limited to the (110) crystal plane, leaving a comprehensive understanding of its electronic structure incomplete [43–46]. Moreover, even within ARPES studies on (110)-oriented single crystals, the results remain highly controversial, with conflicting reports between the paramagnetic (PM) band degeneracy and the altermagnetic band splitting [45, 46]. It is thus highly desirable to carry out the comprehensive ARPES measurements on different surface orientations to clarify the universality and dissimilarity in the surface-dependent electronic states.

In this article, we report a spin-resolved ARPES study with a RuO<sub>2</sub> bulk single crystal which has three different surface planes of (100), (110) and (101), in combination with first-principles calculations, to address the key questions above. We show that the absence of altermagnetic spin splitting is a universal feature irrespective of crystal orientations. We also found energy bands crossing the Fermi level ( $E_F$ ) associated with the surface states (SS) in the ( $E, k$ ) region where no corresponding bands exist in the bulk-band calculation. The effective mass of SS strongly depends on the crystal orientation. We discuss implications of the present results in relation to the topological properties.

## II. EXPERIMENTS AND CALCULATIONS

RuO<sub>2</sub> single crystals were grown by the vapor-transport method in flowing oxygen [47]. Polycrystalline RuO<sub>2</sub> pellets were placed in an alumina tube and heated at 1250°C for 168 hours to yield single crystals of the size up to  $5 \times 3 \times 2$  mm<sup>3</sup> at lower temperature locations.

Obtained crystals were characterized by x-ray diffraction spectra as well as Laue photographs and electrical resistivity. Temperature ( $T$ ) dependence of the electrical resistivity shows a metallic behavior in the whole  $T$  range. Residual resistivity is  $0.1 \text{ } \Omega\text{cm}$  for the current along [001], and the residual resistivity ratio (RRR) reaches 400. This value is the highest level among thus-far reported RRR values for the bulk crystal (20–230) [47–50] and thin films (2–5) [22, 24, 34], confirming the high-quality nature of our single crystal.

ARPES measurements were performed at BL-28A in Photon Factory (PF) with circularly polarized 40–200 eV photons using a micro beam spot of  $12 \times 10 \text{ } \mu\text{m}^2$  [51]. Spin-resolved ARPES measurements were carried out at CASSIOPÉE beamline in SOLEIL with circularly and linear horizontally polarized 46–74 eV photons. Samples were cleaved *in situ* along the (100), (110), and (101) crystal planes in an ultrahigh vacuum of  $\sim 1.0 \times 10^{-10}$  Torr, and the successful cleaving was confirmed by looking at the cleaved surface with optical microscope and by checking the symmetry and periodicity of observed band dispersions and Fermi surface (FS). Sample was kept at  $T = 40 \text{ K}$  during ARPES measurements.

First-principles band-structure calculations were carried out by using the projector augmented wave method implemented in the Vienna *ab initio* simulation package (VASP) code [52]. The SS was obtained with the surface Green’s function method implemented in WannierTools code [53] after the maximally localized Wannier functions for Ru-4*d* and O-2*p* orbital states were obtained by using Wannier90 code [54]. To stabilize the AFM order, we included on-site Coulomb interaction energy  $U = 2.0 \text{ eV}$  for the calculation in the AFM phase, whereas the calculation in the nonmagnetic (NM) phase was obtained without including  $U$ .

### III. ELECTRONIC STRUCTURE FROM (100), (110), AND (101) SURFACES

Although previous ARPES measurements with bulk single crystals and thin films were carried out on the (110) surface [43–46], we found that the bulk crystal can be cleaved nicely also on the (100) and (101) surfaces [indicated by the shaded area in Fig. 1(a)]. These three types of flat surfaces are identified as facets of an as-grown single crystal as shown in Fig. 1(b). We have characterized the orientation of these surfaces by x-ray Laue backscattering measurements [Fig. 1(c)] in which clear and sharp diffraction spots, consistent with the symmetry of each surface, are well recognized.

We first present the band structure and FS with incident photons on the (100) surface

which have not been accessed by previous ARPES studies. This plane has a straightforward relationship with the antiferromagnetic nodal plane. Figure 2(a) shows the calculated bulk FS for the NM (top panel) and AFM (middle and bottom panels) phases. Since the calculation in the PM phase is difficult because of the random alignment of spins, we approximate the experimental PM phase with the NM phase in the calculation. One can immediately recognize several large spin degenerate 3D pockets in the NM phase. On the other hand, the FSs in the AFM phase are spin split due to the antiferromagnetic band splitting. Because of the  $d$ -wave nature, the spin-up and spin-down FSs are rotated by  $90^\circ$  from each other about the  $k_z$  axis, and the band splitting vanishes on both the  $k_x$  or  $k_y = 0.0$  ( $\Gamma$ XRZ) and  $k_x$  or  $k_y = 1.0$  (XMAR) high-symmetry nodal planes. Away from the high-symmetry planes, such as the  $k_x = 0.5$  ( $\Delta$ YTU) plane, the bands are spin split unless the measured  $k$  cut crosses the nodal planes ( $k_y = 0.0$  and  $1.0$ ). Such a dramatic difference in the shape of FSs between the NM and AFM phases (hereafter called NM and AFM calculations, respectively) enables identification of plausible magnetic phases by a direct comparison with the ARPES-derived band structures [12, 15, 22, 55].

Figures 2(b) and 2(c) show the experimental FSs for the (100) surface plotted against the in-plane wave vectors ( $k_y$  and  $k_z$ ) obtained for the  $k_x \sim 0.0$  plane, which are directly compared with the slice of bulk FSs obtained with the NM and AFM calculations, respectively. The ARPES intensity signifies some characteristic features, such as the absence of spectral weight around the R point and complicated intensity distribution around the  $\Gamma$  point. These features have a periodicity of bulk BZ with two-fold symmetry, indicative of the successful cleavage at the (100) surface. As shown in Fig. 2(b), the calculated FSs in the NM phase show an excellent agreement with the ARPES intensity. In particular, rounded triangular pockets (called  $\alpha$ ) around the Z point intersecting along the ZR cut and the absence of FS around the R point seen in the experiment are nicely reproduced in the NM calculation. On the other hand, as shown in Fig. 2(c), the calculated FS in the AFM phase is too simple; it just contains small pockets centered at the  $\Gamma$  and Z points, in contradiction to the ARPES result. We have confirmed by systematically changing the on-site coulomb energy  $U$  in the AFM calculation that the discrepancy between the experiment and AFM calculation is not attributed to the incorrect choice of  $U$  (for details, see Supplementary Note 1).

To obtain further insights into the band structure, we directly examine the experimental band dispersion. Figures 2(d)–2(i) show the ARPES intensity plotted against the in-plane wave vector ( $k_y$  or  $k_z$ ) and binding energy ( $E_B$ ) along high-symmetry  $k$  cuts, obtained at

selected  $k_x$  slices of  $k_x = 1.0$  [Figs. 2(d, e)],  $0.5$  [Figs. 2(f, g)], and  $0.0$  [Figs. 2(h, i)]. These plots signify several dispersive bands. One can make a clear comparison between the ARPES results and band calculations by following the band dispersion indicated as B1. At  $k_x \sim 0$  [Fig. 2(h)], one can recognize a band at  $E_B \sim 0.2$  eV at the X point which disperses upward along the XR cut and crosses  $E_F$  (green circle). This band disperses back toward higher  $E_B$ , crossing  $E_F$  again (green square) and stays at  $E_B \sim 0.5$  eV around the R point. Along the RZ cut, it touches  $E_F$  around the Z point and rapidly disperses toward higher  $E_B$  along the Z $\Gamma$  cut. A direct comparison with the calculated band dispersions in Fig. 2(i) signifies that the NM calculation (black solid curves) semi-quantitatively reproduces the ARPES-derived band dispersion (dark gray open circles); in particular, regarding a shallow hole band topped at slightly above  $E_F$  along the XR cut, producing the  $\beta$  and  $\gamma$  FSs in Fig. 2(b) as well as the hole band topped at slightly above  $E_F$  along the RZ $\Gamma$  cut associated with the  $\alpha$  pocket in Fig. 2(b). On the other hand, the AFM calculation (red and blue dashed curves; they overlap at  $k_x = 0$ ) shows a fatal disagreement with the experiment along the XR cut [Fig. 2(i)]. The hole band which crosses  $E_F$  in the experiment sinks well below  $E_F$  ( $E_B \sim 0.2$  eV) and stays at  $\sim 0.9$  eV at the R point, away from the experimental one ( $\sim 0.5$  eV). Another hole band at the Z point is topped at far ( $\sim 0.2$  eV) above  $E_F$ , indicating overestimation of the Fermi wave vector ( $k_F$ ) along the Z $\Gamma$  cut (red arrow). Moreover, the  $E_F$  crossing of another band midway between Z and  $\Gamma$  in the experiment (green triangle) is not reproduced in the AFM calculation.

We identified an experimental feature which is not reproduced in neither the NM- nor AFM-calculations. That is a nearly flat band in the vicinity of  $E_F$  along the  $\Gamma$ XR and  $\Gamma$ Z cuts in Fig. 2(h) [orange circles in Figs. 2(e), 2(g), and 2(i)]. It is assigned to the SS, as supported by its  $h\nu$ -independent band dispersion and also by our surface-weight calculations (for details, see Supplementary Notes 2 and 3). In fact, the  $h\nu$  invariance at the  $\bar{\Gamma}$  point can be inferred by looking at the commonly identified near- $E_F$  flat band at X,  $\Delta$ , and  $\Gamma$  points in Figs. 2(d), 2(f) and 2(h) all of which are projected onto the  $\bar{\Gamma}$  point in the surface Brillouin zone (BZ), despite a strong intensity modulation due to the matrix-element effect of photoelectron intensity.

The argument above is further corroborated by a comparison of band dispersions at  $k_x \sim 1.0$  between ARPES and calculations in Figs. 2(d) and 2(e). Besides the B1 band, the ARPES intensity along the MA cut signifies another band called B2 which shows Dirac-like crossing with the B1 band around  $E_F$ . This crossing is nicely reproduced by the NM

calculation in the similar  $(E, k)$  region [Fig. 2(e)], and is attributed to the bulk Dirac nodal line (DNL) with the quadruple band degeneracy appearing commonly in rutile oxides [43, 56–58]. Interestingly, the SS shows up from this DNL and resides on one side (left-hand side) of the DNL along the MA cut; we will come back to this point later. Although the AFM calculation also shows a Dirac-crossing behavior at  $E_F$  (open red diamond), its  $k$  point and the energy dispersion corresponding to the B2 band are very different, again supporting the agreement with the NM calculation. As can be seen in Fig. 2(g), the AFM calculation shows the altermagnetic spin splitting at  $k_x = 0.5$  (the off-nodal plane), leading to the doubling of some bands with respect to the NM case. The ARPES intensity in Fig. 2(f) exhibits no clear signature of such band doubling, as inferred from the smooth evolution of spectral features from  $k_x = 0$  [Fig. 2(h)] to 1.0 [Fig. 2(d)] through  $k_x = 0.5$  [Fig. 2(f)]. We carried out spin-resolved ARPES measurements at  $k$  points where the altermagnetic band splitting is theoretically predicted [red line in Fig. 2(f)], but found that the spin polarization for the bulk bands always keeps zero within experimental uncertainty (for details, see Supplementary Note 4). All these results indicate that the electronic structure of the (100) surface does not support the altermagnetic band splitting.

We found that the ARPES data for the (110) surface [see Fig. 3(a)] share several common features with the (100) surface. The FS mapping against the in-plane wave vectors in Fig. 3(b) obtained in the  $k_{[110]} \sim 0$  plane [ $\Gamma$ ZAM plane; red-shaded plane in Fig. 3(a)] signifies a two-fold-symmetric intensity pattern with the periodicity obeying that of the bulk BZ, consistent with the previous reports [43–46]. A side-by-side comparison of the FS mapping with the NM and AFM calculations in Figs. 3(b) and 3(c), respectively, signifies that the overall FS shape surrounding the  $\Gamma$  point is reproduced well by the NM calculation whereas the size of  $\Gamma$ -centered FS in the AFM calculation is much smaller than that of the experiment. The ARPES intensity shown in Fig. 3(d) along the  $\Gamma$ ZAM $\Gamma$  cut signifies several dispersive bands. Comparison of the ARPES-derived band dispersion with the calculated band dispersions for the NM and AFM cases in Fig. 3(e) reveals that the  $(E, k)$  position of experimental bands are semi-quantitatively reproduced in the NM calculation, whereas the AFM calculation apparently shows a mismatch in the energy position. Similarly to the case of the (100) surface, we found evidence for a flat SS around the  $\Gamma$  point with its surface nature suggested from the  $h\nu$ -invariance of the peak position as shown in Fig. 3(f). It is remarked here that the previous ARPES study supporting the altermagnetic band splitting [46] attributed this flat band to the flat band at 0.4 eV seen in the AFM calculation along



the FM cut (red dashed line) by largely shifting the calculated  $E_F$  position downward, while this amount of energy shift is unrealistic taking into account of nearly stoichiometric nature of the RuO<sub>2</sub> single crystal.

Now we turn our attention to the ARPES results for the (101) surface. As shown in Fig. 4(a), the (101) surface is largely tilted from the nodal planes of the antiferromagnetic spin splitting. Figure 4(b) displays the FS mapping in the  $k_{[101]} \sim 0$  plane, corresponding to the  $\Gamma$ XVW plane [see right top panel of Fig. 4(a)]. One can recognize a prominent intensity pattern following the symmetry and periodicity of the (101) surface, such as hexagonal and ellipsoidal pockets (dashed curves, called  $\delta$  and  $\varepsilon$ ) centered at the  $\Gamma$  point, a small diamond-shaped pocket at the X point ( $\kappa$ ), and X-shaped pattern ( $\lambda$ ) around the V point. A direct comparison of the ARPES intensity with the NM and AFM calculations in Figs. 4(b) and 4(c), respectively, signifies that the calculated FS in the AFM phase simply contains elongated pockets centered at the  $\Gamma$  point, showing a disagreement with the ARPES intensity, whereas the calculated FS in the NM phase shows a better agreement with the experiment.

To clarify the band character, we show in Figs. 4(d) and 4(f) the ARPES intensity along representative  $k$  cuts in the  $k_{[101]} \sim 0.0$  and 1.0 planes, respectively, compared with the corresponding band dispersions obtained by the NM and AFM calculations in Figs. 4(e) and 4(g). One can recognize in Figs. 4(d) and 4(f) several dispersive bands, some of which cross  $E_F$  to contribute to the pockets seen in Figs. 4(b) and 4(c). Although the distinction of more appropriate calculation (NM or AFM) is difficult compared to other surface planes, the experimental broad feature at  $\sim 0.3$ – $0.6$  eV along the RAAR cut in Fig. 4(f) appears to show a better agreement with the NM calculation in Fig. 4(g). Besides these bulk-originated features, one can find in both Figs. 4(d) and 4(f) several dispersive features within  $E_B \sim 0.3$  eV of  $E_F$ , while they have no counterparts in the calculation. For example, an inner electron band that produces the hexagonal  $\delta$  pocket in Fig. 4(b) appears in the  $(E, k)$  region where the calculated bands in the NM phase are absent. This band displays no band dispersion along the out-of-plane wave vector,  $k_{[101]}$  [Figs. 4(d) and 4(f)], supporting its surface origin. One can also recognize a hole band producing a small pocket at the X point associated with the  $\kappa$  pocket in Fig. 4(b). This band is not predicted by the NM calculation and has no dispersion along  $k_{[101]}$  in the experiment [Fig. 4(g)], and hence, it is also attributed to the SS. Therefore, the (101) surface of RuO<sub>2</sub> hosts several dispersive SS that contribute to the formation of surface-derived FS. It is noted here that the inclusion of SOC in the NM calculation slightly improves the matching between the experiment and calculation (see

Supplementary Note 5), but a fatal disagreement is still found in the AFM calculation even when the SOC is included.

#### IV. TOPOLOGICAL SURFACE STATES

Here we summarize our key findings to discuss the implications of present results. We have succeeded in experimentally clarifying the band structure and FS of RuO<sub>2</sub> for multiple crystal orientations, and found that the experimental band structure always shows a better agreement with the NM calculation compared to the AFM calculation irrespective of the crystal orientations. Furthermore, our spin-ARPES measurements definitively show no evidence for the spin polarization of the bulk bands. The present study supports the absence of antiferromagnetism and altermagnetic band splitting in bulk single crystal of RuO<sub>2</sub>, settling the fierce debates on the altermagnetic nature of RuO<sub>2</sub>, at least for the bulk crystal (note that, at the moment, we do not exclude the possibility that a RuO<sub>2</sub> thin film shows altermagnetic behavior, because the crystal defects and lattice strain are not the same as those of bulk crystal). We also found that the existence of SS is a common characteristic of RuO<sub>2</sub> irrespective of the crystal orientation, while its energy dispersion on the (101) surface shows dispersive characteristics distinct from those of the (100) and (110) surfaces hosting nearly flat SS around  $E_F$ .

We propose that the key characteristics of SS observed at the three different crystal orientations are commonly explained in terms of the existence of DNL in bulk bands and associated topological SS. First-principles calculations for rutile oxides (RuO<sub>2</sub>, IrO<sub>2</sub> and OsO<sub>2</sub>) [56] predicted the existence of bulk DNL accompanying topological SS [43, 57, 58], which is located at around a specific  $k_z$  plane ( $\sim 2/3$  in the unit of  $\pi/c$ ; called here the DNL plane) and extends along the  $k_{[110]}$  and  $k_{[1\bar{1}0]}$  axes as shown in Fig. 3(a). Actually, the SOC lifts the degeneracy of Dirac node by  $\sim 0.1$  eV and contributes to the spin Berry curvature [56]; see also Figs. S5(a) and S5(b). Being associated with this DNL, a large volume of  $k$  region in bulk BZ (region with  $k_z \lesssim 2/3$ ; indicated by red dashed box) including the  $\Gamma$ , X, and M points becomes a band-inverted region, whereas the remaining smaller region with  $k_z \gtrsim 2/3$  including the Z, A, and R points is not inverted. Since the (100) and (110) planes vertically intersect the DNL plane, one can distinguish between inverted and non-inverted  $k$  regions in the projected surface BZ. Namely, the topological SS is expected to emerge in the  $k$  cut which crosses the surface projection of bulk  $\Gamma$ , X, and M points, whereas it is absent

in the  $k$  cut connecting the surface projection of the bulk Z, R, and A lines.

We found that the observed SS exactly follows the above trend. Specifically, at the (100) surface, the SS appears along the XM, MA, and XR cuts, but not along the AR cut as seen in Fig. 2(d). Similarly, it appears along the  $\Gamma$ X, XR, and  $\Gamma$ Z cuts, but not along the ZR cut as seen in Fig. 2(h). At the (110) surface [Fig. 3(d)], the SS appears along the  $\Gamma$ Z, AM, and  $\Gamma$ M cuts, but not along the ZA cut. These arguments are also supported by the FS mapping in Figs. 2(a) and 3(b) where the overall intensity in the band-inverted area of  $|k_z| \lesssim 2/3$  is relatively enhanced due to the presence of SS. This is also corroborated by slab calculations detailed in Supplementary Note 3.

In contrast to the (100) and (110) planes, the (101) plane intersects the DNL plane with  $34.9^\circ$ , so that the surface projection of inverted region covers the whole region of the (101) surface BZ. This situation makes it difficult to predict the actual  $k$  location of SS and is also likely responsible for a more dispersive nature of the SS in the (101) surface compared to the (100) and (110) planes in which relationship between the  $(E, k)$  locations of the DNL and associated SS is more straightforward. We thus infer that the SS appearing ubiquitously in all the three crystal orientations is a reflection of its topological nature associated with the bulk-band inversion in a wide 3D  $k$  space, and strongly affects the surface characteristics of RuO<sub>2</sub> such as spectroscopic, transport, and chemical properties. In this regard, it is worthwhile to comment on the possibility that the catalytic reaction particularly known for the (110) surface [40] may be promoted by the existence of topological SS [43], because high surface conductivity and robustness of the topological SS would be useful for the catalytic reaction [59, 60], working as a “topological catalyst”. In RuO<sub>2</sub>, the proximity of the topological SS to  $E_F$  [ $\sim 20$  meV ( $\sim 200$  K) of  $E_F$ ; see Fig. 3(f)] for the (110) and (100) surfaces would promote catalytic reaction at room temperature.

While the present study focuses on the surface of bulk crystal, it would be natural to extend our arguments to the interface between RuO<sub>2</sub> (including RuO<sub>2</sub> thin film) and other materials. The present study suggests that the outstanding transport properties of RuO<sub>2</sub> thin film such as the spin-charge conversion (spin splitting torque) and other physical properties that involve charge/spin transport across the interface should be discussed with taking into account the existence of prominent topological interface states besides the bulk DNL that strongly contributes to the spin Berry curvature [30, 56]. In other words, we caution that a theoretical model that simply deals with the altermagnetic splitting of bulk bands without incorporating the topological surface/interface states and bulk DNL is insufficient

to fully account for some of the experimental results of RuO<sub>2</sub>.

## V. CONCLUSION

The present micro-ARPES study, in collaboration with first-principles calculations, for three different crystal orientations of bulk RuO<sub>2</sub> crystal has revealed the absence of antiferromagnetic band splitting. Besides the bulk-band degeneracy, we observed a topological surface states near  $E_F$  associated with the bulk Dirac nodal lines irrespective of the crystal orientation. Intriguingly, its characteristics, i.e. the flat vs dispersive nature, was found to be strongly crystal-orientation dependent. The present results imply important roles of the importance of topological surface and interface states to account for the exotic physical and chemical properties of RuO<sub>2</sub>.

## ACKNOWLEDGMENTS

We acknowledge G. Mattoni, H. Matsuki, and C. Sow for their technical supports. We also acknowledge L. Balents and J. N. Hausman for useful comments and discussions. This work was supported by JST-CREST (No. JPMJCR18T1), Grant-in-Aid for Scientific Research (JSPS KAKENHI Grant Numbers JP22H01168, JP21H04435 and JP19H01845), Grant-in-Aid for JSPS Research Fellow (No: JP18J20058), and KEK-PF (Proposal number: 2024S2-001). T. Osumi thanks GP-Spin and A.H. thanks GP-Spin and JSPS for financial support.

- 
- [1] Y. A. Bychkov and E. I. Rashba, Properties of a 2D electron gas with lifted spectral degeneracy, *P. Zh. Eksp. Teor. Fiz.* **39**, 66 (1984).
  - [2] G. Dresselhaus, Spin-Orbit Coupling Effects in Zinc Blende Structures, *Phys. Rev.* **100**, 580 (1955).
  - [3] S. Murakami, N. Nagaosa, and S.-C. Zhang, Dissipationless Quantum Spin Current at Room Temperature, *Science* **301**, 1348 (2003).
  - [4] J. Sinova, D. Culcer, Q. Niu, N. A. Sinitsyn, T. Jungwirth, and A. H. MacDonald, Universal Intrinsic Spin Hall Effect, *Physical Review Letters* **92**, 126603 (2004).
  - [5] Y. K. Kato, R. C. Myers, A. C. Gossard, and D. D. Awschalom, Observation of the spin hall effect in semiconductors, *Science* **306**, 1910 (2004).

- [6] J. Sinova, S. O. Valenzuela, J. Wunderlich, C. H. Back, and T. Jungwirth, Spin Hall effects, [Reviews of Modern Physics](#) **87**, 1213 (2015).
- [7] M. Sigrist, Introduction to unconventional superconductivity in non-centrosymmetric metals, [AIP Conference Proceedings](#) **1162**, 55 (2009).
- [8] S. Yip, Noncentrosymmetric Superconductors, [Annual Review of Condensed Matter Physics](#) **5**, 15 (2014).
- [9] A. Daido, Y. Ikeda, and Y. Yanase, Intrinsic Superconducting Diode Effect, [Physical Review Letters](#) **128**, 037001 (2022).
- [10] N. F. Q. Yuan and L. Fu, Supercurrent diode effect and finite-momentum superconductors, [Proceedings of the National Academy of Sciences](#) **119**, e 2119548119 (2022).
- [11] F. Ando, Y. Miyasaka, T. Li, J. Ishizuka, T. Arakawa, Y. Shiota, T. Moriyama, Y. Yanase, and T. Ono, Observation of superconducting diode effect, [Nature](#) **584**, 373 (2020).
- [12] K. H. Ahn, A. Hariki, K. W. Lee, and J. Kuneš, Antiferromagnetism in RuO<sub>2</sub> as *d*-wave Pomeranchuk instability, [Physical Review B](#) **99**, 184432 (2019).
- [13] M. Naka, S. Hayami, H. Kusunose, Y. Yanagi, Y. Motome, and H. Seo, Spin current generation in organic antiferromagnets, [Nature Communications](#) **10**, 4305 (2019).
- [14] S. Hayami, Y. Yanagi, and H. Kusunose, Momentum-Dependent Spin Splitting by Collinear Antiferromagnetic Ordering, [Journal of the Physical Society of Japan](#) **88**, 123702 (2019).
- [15] L. Šmejkal, R. González-Hernández, T. Jungwirth, and J. Sinova, Crystal time-reversal symmetry breaking and spontaneous Hall effect in collinear antiferromagnets, [Science Advances](#) **6**, eaaz8809 (2020).
- [16] L.-D. Yuan, Z. Wang, J.-W. Luo, E. I. Rashba, and A. Zunger, Giant momentum-dependent spin splitting in centrosymmetric low-Z antiferromagnets, [Physical Review B](#) **102**, 014422 (2020).
- [17] L.-D. Yuan, Z. Wang, J.-W. Luo, and A. Zunger, Prediction of low-Z collinear and noncollinear antiferromagnetic compounds having momentum-dependent spin splitting even without spin-orbit coupling, [Physical Review Materials](#) **5**, 014409 (2021).
- [18] H.-Y. Ma, M. Hu, N. Li, J. Liu, W. Yao, J.-F. Jia, and J. Liu, Multifunctional antiferromagnetic materials with giant piezomagnetism and noncollinear spin current, [Nature Communications](#) **12**, 2846 (2021).
- [19] L. Šmejkal, J. Sinova, and T. Jungwirth, Beyond Conventional Ferromagnetism and Antiferromagnetism: A Phase with Nonrelativistic Spin and Crystal Rotation Symmetry, [Physical](#)

- [Review X \*\*12\*\*, 031042 \(2022\)](#).
- [20] L. Šmejkal, J. Sinova, and T. Jungwirth, Emerging Research Landscape of Altermagnetism, [Physical Review X \*\*12\*\*, 040501 \(2022\)](#).
- [21] R. González-Hernández, L. Šmejkal, K. Výborný, Y. Yahagi, J. Sinova, T. Jungwirth, and J. Železný, Efficient Electrical Spin Splitter Based on Nonrelativistic Collinear Antiferromagnetism, [Physical Review Letters \*\*126\*\*, 127701 \(2021\)](#).
- [22] Z. Feng, X. Zhou, L. Šmejkal, L. Wu, Z. Zhu, H. Guo, R. González-Hernández, X. Wang, H. Yan, P. Qin, X. Zhang, H. Wu, H. Chen, Z. Meng, L. Liu, Z. Xia, J. Sinova, T. Jungwirth, and Z. Liu, An anomalous Hall effect in altermagnetic ruthenium dioxide, [Nature Electronics \*\*5\*\*, 735 \(2022\)](#).
- [23] H. Bai, L. Han, X. Y. Feng, Y. J. Zhou, R. X. Su, Q. Wang, L. Y. Liao, W. X. Zhu, X. Z. Chen, F. Pan, X. L. Fan, and C. Song, Observation of Spin Splitting Torque in a Collinear Antiferromagnet RuO<sub>2</sub>, [Physical Review Letters \*\*128\*\*, 197202 \(2022\)](#).
- [24] S. Karube, T. Tanaka, D. Sugawara, N. Kadoguchi, M. Kohda, and J. Nitta, Observation of Spin-Splitter Torque in Collinear Antiferromagnetic RuO<sub>2</sub>, [Physical Review Letters \*\*129\*\*, 137201 \(2022\)](#).
- [25] A. Bose, N. J. Schreiber, R. Jain, D.-F. Shao, H. P. Nair, J. Sun, X. S. Zhang, D. A. Muller, E. Y. Tsymlal, D. G. Schlom, and D. C. Ralph, Tilted spin current generated by the collinear antiferromagnet ruthenium dioxide, [Nature Electronics \*\*5\*\*, 267 \(2022\)](#).
- [26] H. Bai, Y. C. Zhang, Y. J. Zhou, P. Chen, C. H. Wan, L. Han, W. X. Zhu, S. X. Liang, Y. C. Su, X. F. Han, F. Pan, and C. Song, Efficient Spin-to-Charge Conversion via Altermagnetic Spin Splitting Effect in Antiferromagnet RuO<sub>2</sub>, [Physical Review Letters \*\*130\*\*, 216701 \(2023\)](#).
- [27] T. Tschirner, P. Keßler, R. D. G. Betancourt, T. Kotte, D. Kriegner, B. Büchner, J. Dufouleur, M. Kamp, V. Jovic, L. Smejkal, J. Sinova, R. Claessen, T. Jungwirth, S. Moser, H. Reichlova, and L. Veyrat, Saturation of the anomalous Hall effect at high magnetic fields in altermagnetic RuO<sub>2</sub>, [APL Materials \*\*11\*\*, 101103 \(2023\)](#).
- [28] M. Wang, K. Tanaka, S. Sakai, Z. Wang, K. Deng, Y. Lyu, C. Li, D. Tian, S. Shen, N. Ogawa, N. Kanazawa, P. Yu, R. Arita, and F. Kagawa, Emergent zero-field anomalous Hall effect in a reconstructed rutile antiferromagnetic metal, [Nature Communications \*\*14\*\*, 8240 \(2023\)](#).
- [29] Y. Guo, J. Zhang, Z. Zhu, Y. yuan Jiang, L. Jiang, C. Wu, J. Dong, X. Xu, W. He, B. He, Z. Huang, L. Du, G. Zhang, K. Wu, X. Han, D. fu Shao, G. Yu, and H. Wu, Direct and Inverse Spin Splitting Effects in Altermagnetic RuO<sub>2</sub>, [Advanced Science \*\*11\*\*, 2400967 \(2024\)](#).

- [30] Z. Wang, Z. Li, L. Sun, Z. Zhang, K. He, H. Niu, J. Cheng, M. Yang, X. Yang, G. Chen, Z. Yuan, H. Ding, and B. Miao, Inverse Spin Hall Effect Dominated Spin-Charge Conversion in (101) and (110)-Oriented RuO<sub>2</sub> Films, [Physical Review Letters \*\*133\*\*, 046701 \(2024\)](#).
- [31] S. G. Jeong, I. H. Choi, S. Nair, L. Buiarelli, B. Pourbahari, J. Y. Oh, N. Bassim, A. Seo, W. S. Choi, R. M. Fernandes, T. Birol, L. Zhao, J. S. Lee, and B. Jalan, Altermagnetic Polar Metallic phase in Ultra-Thin Epitaxially-Strained RuO<sub>2</sub> Films, [arXiv:2405.05838 \(2024\)](#).
- [32] T. Berlijn, P. Snijders, O. Delaire, H.-D. Zhou, T. Maier, H.-B. Cao, S.-X. Chi, M. Matsuda, Y. Wang, M. Koehler, P. Kent, and H. Weitering, Itinerant Antiferromagnetism in RuO<sub>2</sub>, [Physical Review Letters \*\*118\*\*, 077201 \(2017\)](#).
- [33] Z. H. Zhu, J. Stremper, R. R. Rao, C. A. Occhialini, J. Pellicciari, Y. Choi, T. Kawaguchi, H. You, J. F. Mitchell, Y. Shao-Horn, and R. Comin, Anomalous Antiferromagnetism in Metallic RuO<sub>2</sub> Determined by Resonant X-ray Scattering, [Physical Review Letters \*\*122\*\*, 17202 \(2019\)](#).
- [34] B. Z. Gregory, J. Stremper, D. Weinstock, J. P. Ruf, Y. Sun, H. Nair, N. J. Schreiber, D. G. Schlom, K. M. Shen, and A. Singer, Strain-induced orbital-energy shift in antiferromagnetic RuO<sub>2</sub> revealed by resonant elastic x-ray scattering, [Physical Review B \*\*106\*\*, 195135 \(2022\)](#).
- [35] X. Zhou, W. Feng, R.-W. Zhang, L. Šmejkal, J. Sinova, Y. Mokrousov, and Y. Yao, Crystal Thermal Transport in Altermagnetic RuO<sub>2</sub>, [Physical Review Letters \*\*132\*\*, 056701 \(2024\)](#).
- [36] D. F. Shao, S. H. Zhang, M. Li, C. B. Eom, and E. Y. Tsymbal, Spin-neutral currents for spintronics, [Nature Communications \*\*12\*\*, 7061 \(2021\)](#).
- [37] D. F. Shao, Y. Y. Jiang, J. Ding, S. H. Zhang, Z. A. Wang, R. C. Xiao, G. Gurung, W. J. Lu, Y. P. Sun, and E. Y. Tsymbal, Néel Spin Currents in Antiferromagnets, [Physical Review Letters \*\*130\*\*, 1 \(2023\)](#).
- [38] Y. Liu, H. Bai, Y. Song, Z. Ji, S. Lou, Z. Zhang, C. Song, and Q. Jin, Inverse Altermagnetic Spin Splitting Effect-Induced Terahertz Emission in RuO<sub>2</sub>, [Advanced Optical Materials \*\*11\*\*, 2300177 \(2023\)](#).
- [39] S. Zhang, Y. Cui, S. Wang, H. Chen, Y. Liu, W. Qin, T. Guan, C. Tian, Z. Yuan, L. Zhou, Y. Wu, and Z. Tao, Nonrelativistic and nonmagnetic terahertz-wave generation via ultrafast current control in anisotropic conductive heterostructures, [Advanced Photonics \*\*5\*\*, 056006 \(2023\)](#).
- [40] H. Over, Y. D. Kim, A. P. Seitsonen, S. Wendt, E. Lundgren, M. Schmid, P. Varga, A. Morgante, and G. Ertl, Atomic-Scale Structure and Catalytic Reactivity of the RuO<sub>2</sub> (110) Surface,

- [Science](#) **287**, 1474 (2000).
- [41] M. Hiraishi, H. Okabe, A. Koda, R. Kadono, T. Muroi, D. Hirai, and Z. Hiroi, Nonmagnetic Ground State in RuO<sub>2</sub> Revealed by Muon Spin Rotation, [Physical Review Letters](#) **132**, 166702 (2024).
- [42] P. Keßler, L. Garcia-Gassull, A. Suter, T. Prokscha, Z. Salman, D. Khalyavin, P. Manuel, F. Orlandi, I. I. Mazin, R. Valentı, and S. Moser, Absence of magnetic order in RuO<sub>2</sub>: insights from  $\mu$ SR spectroscopy and neutron diffraction, [arXiv:2405.10820](#) (2024).
- [43] V. Jovic, R. J. Koch, S. K. Panda, H. Berger, P. Bugnon, A. Magrez, K. E. Smith, S. Biermann, C. Jozwiak, A. Bostwick, E. Rotenberg, and S. Moser, Dirac nodal lines and flat-band surface state in the functional oxide RuO<sub>2</sub>, [Physical Review B](#) **98**, 241101(R) (2018).
- [44] O. Fedchenko, J. Minár, A. Akashdeep, S. W. D’Souza, D. Vasilyev, O. Tkach, L. Odenbreit, Q. Nguyen, D. Kutnyakhov, N. Wind, L. Wenthau, M. Scholz, K. Rossnagel, M. Hoesch, M. Aeschlimann, B. Stadtmüller, M. Kläui, G. Schönhense, T. Jungwirth, A. B. Hellenes, G. Jakob, L. Šmejkal, J. Sinova, and H.-J. Elmers, Observation of time-reversal symmetry breaking in the band structure of altermagnetic RuO<sub>2</sub>, [Science Advances](#) **10**, eadj4883 (2024).
- [45] J. Liu, J. Zhan, T. Li, J. Liu, S. Cheng, Y. Shi, L. Deng, M. Zhang, C. Li, J. Ding, Q. Jiang, M. Ye, Z. Liu, Z. Jiang, S. Wang, Q. Li, Y. Xie, Y. Wang, S. Qiao, J. Wen, Y. Sun, and D. Shen, Absence of Altermagnetic Spin Splitting Character in Rutile Oxide RuO<sub>2</sub>, [Physical Review Letters](#) **133**, 176401 (2024).
- [46] Z. Lin, D. Chen, W. Lu, X. Liang, S. Feng, K. Yamagami, J. Osiecki, M. Leandersson, B. Thiagarajan, J. Liu, C. Felser, and J. Ma, Observation of Giant Spin Splitting and *d*-wave Spin Texture in Room Temperature Altermagnet RuO<sub>2</sub>, [arXiv:2402.04995](#) (2024).
- [47] Y. Huang, H. Park, and F. H. Pollak, Growth and characterization of RuO<sub>2</sub> single crystals, [Materials Research Bulletin](#) **17**, 1305 (1982).
- [48] D. B. Rogers, R. D. Shannon, A. W. Sleight, and J. L. Gillson, Crystal chemistry of metal dioxides with rutile-related structures, [Inorganic Chemistry](#) **8**, 841 (1969).
- [49] W. D. Ryden, A. W. Lawson, and C. C. Sartain, Electrical transport properties of IrO<sub>2</sub> and RuO<sub>2</sub>, [Physical Review B](#) **1**, 1494 (1970).
- [50] F. Pawula, A. Fakih, R. Daou, S. Hébert, N. Mordvinova, O. Lebedev, D. Pelloquin, and A. Maignan, Multiband transport in RuO<sub>2</sub>, [Physical Review B](#) **110**, 064432 (2024).
- [51] M. Kitamura, S. Souma, A. Honma, D. Wakabayashi, H. Tanaka, A. Toyoshima, K. Amemiya, T. Kawakami, K. Sugawara, K. Nakayama, K. Yoshimatsu, H. Kumigashira, T. Sato, and



- K. Horiba, Development of a versatile micro-focused angle-resolved photoemission spectroscopy system with Kirkpatrick–Baez mirror optics, *Review of Scientific Instruments* **93**, 033906 (2022).
- [52] G. Kresse and J. Furthmüller, Efficient iterative schemes for ab initio total-energy calculations using a plane-wave basis set, *Physical Review B* **54**, 11169 (1996).
- [53] Q. Wu, S. Zhang, H.-F. Song, M. Troyer, and A. A. Soluyanov, WannierTools: An open-source software package for novel topological materials, *Computer Physics Communications* **224**, 405 (2018).
- [54] A. A. Mostofi, J. R. Yates, Y.-S. Lee, I. Souza, D. Vanderbilt, and N. Marzari, wannier90: A tool for obtaining maximally-localised Wannier functions, *Computer Physics Communications* **178**, 685 (2008).
- [55] A. Smolyanyuk, I. I. Mazin, L. Garcia-Gassull, and R. Valentí, Fragility of the magnetic order in the prototypical altermagnet RuO<sub>2</sub>, *Physical Review B* **109**, 134424 (2024).
- [56] Y. Sun, Y. Zhang, C.-X. Liu, C. Felser, and B. Yan, Dirac nodal lines and induced spin Hall effect in metallic rutile oxides, *Physical Review B* **95**, 235104 (2017).
- [57] X. Xu, J. Jiang, W. J. Shi, V. Süß, C. Shekhar, S. C. Sun, Y. J. Chen, S.-K. Mo, C. Felser, B. H. Yan, H. F. Yang, Z. K. Liu, Y. Sun, L. X. Yang, and Y. L. Chen, Strong spin-orbit coupling and Dirac nodal lines in the three-dimensional electronic structure of metallic rutile IrO<sub>2</sub>, *Physical Review B* **99**, 195106 (2019).
- [58] J. N. Nelson, J. P. Ruf, Y. Lee, C. Zeledon, J. K. Kawasaki, S. Moser, C. Jozwiak, E. Rotenberg, A. Bostwick, D. G. Schlom, K. M. Shen, and L. Moreschini, Dirac nodal lines protected against spin-orbit interaction in IrO<sub>2</sub>, *Physical Review Materials* **3**, 064205 (2019).
- [59] G. Li, Q. Xu, W. Shi, C. Fu, L. Jiao, M. E. Kamminga, M. Yu, H. Tüysüz, N. Kumar, V. Süß, R. Saha, A. K. Srivastava, S. Wirth, G. Aufermann, J. Gooth, S. Parkin, Y. Sun, E. Liu, and C. Felser, Surface states in bulk single crystal of topological semimetal Co<sub>3</sub>Sn<sub>2</sub>S<sub>2</sub> toward water oxidation, *Science Advances* **5**, eaaw9867 (2019).
- [60] G. Li, C. Fu, W. Shi, L. Jiao, J. Wu, Q. Yang, R. Saha, M. E. Kamminga, A. K. Srivastava, E. Liu, A. N. Yazdani, N. Kumar, J. Zhang, G. R. Blake, X. Liu, M. Fahlman, S. Wirth, G. Aufermann, J. Gooth, S. Parkin, V. Madhavan, X. Feng, Y. Sun, and C. Felser, Dirac Nodal Arc Semimetal PtSn<sub>4</sub>: An Ideal Platform for Understanding Surface Properties and Catalysis for Hydrogen Evolution, *Angewandte Chemie International Edition* **58**, 13107 (2019).

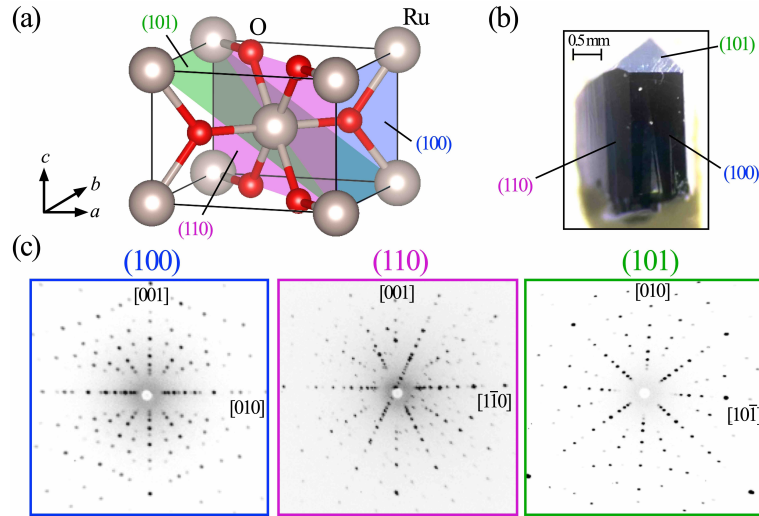


FIG. 1. **X-ray characterization of RuO<sub>2</sub> crystal on different surface planes.** (a), (b) Crystal structure and photograph of a typical RuO<sub>2</sub> single crystal, respectively. (c) X-ray Laue images for (100), (110), and (101) surfaces [shaded areas in (a)].

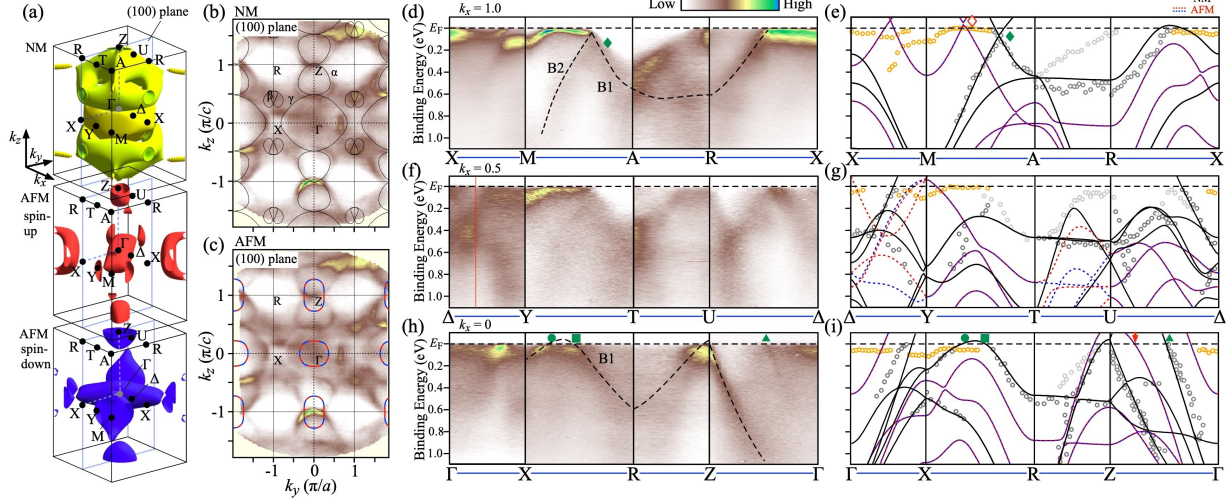


FIG. 2. **ARPES spectra obtained from the (100) surface of RuO<sub>2</sub> crystal.** (a) Calculated FSs obtained by (top) NM calculation, and AFM calculation for (middle) spin up and (bottom) spin-down states. In the calculation for the AFM phase, we neglected the SOC. (b), (c) FS mapping at  $T = 40$  K for the (100) surface at  $k_x = 0.0$  obtained with  $h\nu = 110$  eV, overlaid with the FS obtained by NM and AFM calculations, respectively. Spin-up and spin-down FSs in (c) indicated by red/blue dashed curves completely overlap in this plane. (d), (e) ARPES-intensity plot obtained along the principal  $k$  cut (XMARX cut) at  $k_x = 1.0$  (in the unit of  $\pi/a$ ) and corresponding calculated band dispersions. Black solid curves are for the NM phase, and red/blue dashed curves (they overlap along this  $k$  cut) are for the AFM phase. Dashed curves in (d) are guides to the eye to trace the experimental band dispersion. Experimental band dispersions extracted by tracing the peak position in energy distribution curves (EDCs) are indicated by open circles in (e). Note that broad feature dispersing toward  $E_F$  on moving from A to R (light gray circles) may be attributed to the B1 band from the  $k_x \sim 0$  plane that appears due to the momentum broadening along the wave vector perpendicular to the (100) plane, associated with the short photoelectron mean-free path. (f, g), (h, i) Same as (d), (e) but obtained at  $k_x = 0.5$  and  $0.0$ , respectively. Light gray circles in (e), (g), and (i) highlight features which may originate from the spectral broadening along the wave vector perpendicular to the (100) plane. Orange circles highlight possible SS.

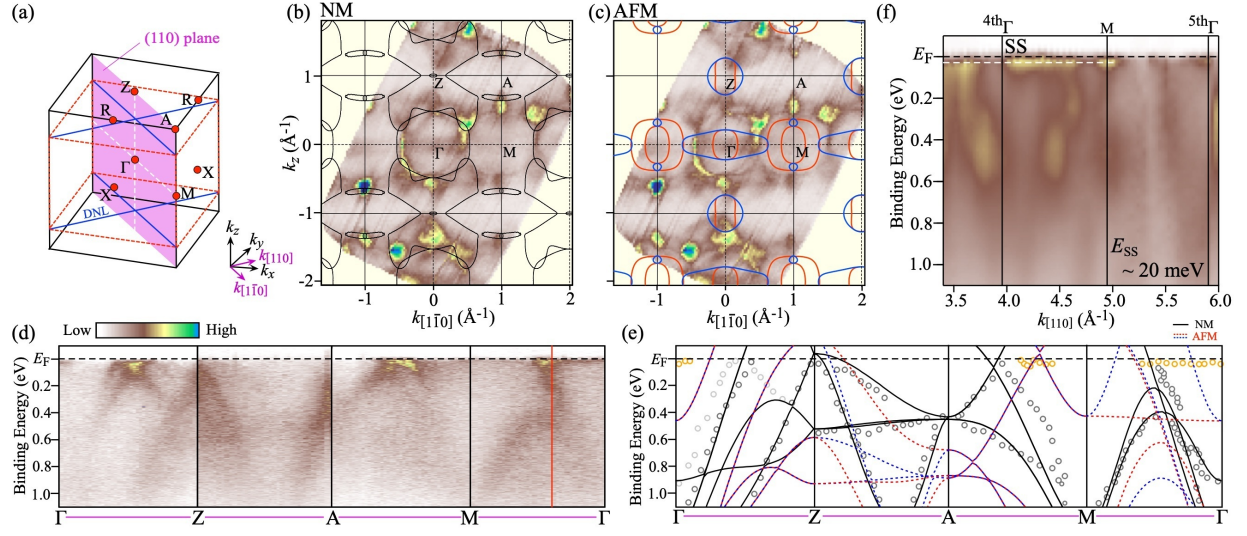


FIG. 3. **ARPES spectra obtained from the (110) surface of RuO<sub>2</sub> crystal.** (a) Bulk BZ and  $k$  plane ( $k_{[110]} = 0.0$ ) where the FS mapping shown in (b) and (c) was obtained. Blue lines represent DNL predicted by the DFT calculation [56]. For simplicity, DNL are depicted as straight lines. Region enclosed by the DNL, i.e. bulk-band-inverted  $k$  region, is indicated by red dashed box. (b), (c) FS mapping at the (110) surface obtained at  $k_{[110]} = 0.0$  with  $h\nu = 126$  eV, overlaid with the calculated FS obtained by NM (b) and AFM (c) calculations. (d) ARPES intensity plotted against  $E_B$  and wave vector along the  $\Gamma Z A M \Gamma$  cut. (e) ARPES-derived band dispersion (open circles) overlaid with the calculated band dispersions obtained by the NM calculation (black curves) and AFM calculation (red and blue dashed curves). The ARPES results are explained well with the NM calculation, but sharply disagree with the AFM calculation. (f) Normal-emission ARPES intensity plotted against  $E_B$  and wave vector along the  $k_{[110]}$  axis. SS refers to the surface states.

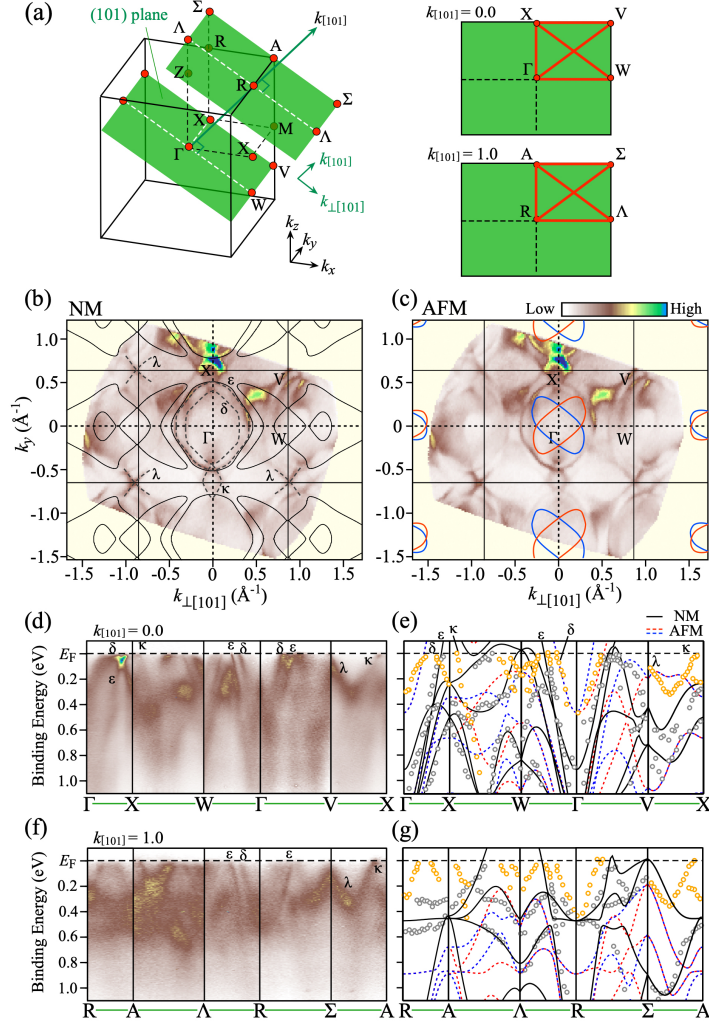


FIG. 4. ARPES spectra obtained from the (101) surface of RuO<sub>2</sub> crystal. (a) Bulk BZ and  $k$  planes ( $k_{[101]} = 0.0$  and  $1.0$ ) in which the FS mapping and ARPES intensity shown in (b)–(g) were obtained. Right panels indicate the  $k$  cuts (red solid lines) where the ARPES-intensity plots in (d) and (f) are obtained. Note that V, W,  $\Sigma$ , and  $\Lambda$  points are note the high-symmetry points. (b), (c) FS mapping at the (101) surface at  $k_{[101]} = 0.0$  at  $h\nu = 83$  eV, overlaid with the FS obtained by the NM and AFM calculations, respectively. Red and blue curves in (c) represent spin-up and spin-down FSs. Note that the calculated FS in the NM phase shows a better agreement with the experiment, in particular, regarding the presence of  $\varepsilon$  pocket and the existence of FS around the W point. A careful look further reveals that the experimental  $\delta$ ,  $\kappa$ , and  $\lambda$  FSs show no counterparts in the calculation, suggesting their SS origin. (d), (e) ARPES-intensity plot obtained along the principle  $k$  cut ( $\Gamma$ XWTVX cut) at  $k_{[101]} = 0.0$  and corresponding calculated band dispersions in the NM (black solid curves) and AFM (red and blue dashed curves) phases, respectively. Experimental band dispersions are shown by open circles in (e). (f), (g) Same as (d) and (e) but measured along the RAAR $\Sigma$ A cut at  $k_{[101]} = 1.0$ .

**Supplemental Note 1: Hubbard  $U$  dependence of the calculated band structure.**

To clarify the influence of on-site Coulomb interaction energy (Hubbard  $U$ ) on the calculated Fermi surface (FS) and band structure in the antiferromagnetic (AFM) phase, we compare in Figs. S1(a)–S1(c) and S1(d)–S1(f) the FS in the two-dimensional wave vector and the ARPES-derived band dispersion, respectively, for the (100) surface of RuO<sub>2</sub> at  $k_x = 0$  at three different  $U$  values of 1.5, 2.0, and 2.5 eV. We found from our calculations that the AFM phase is energetically more stable than the nonmagnetic (NM) phase at  $U \geq 2.0$  eV, whereas *vice versa* for  $U = 1.5$  eV. Hence, the calculation for  $U = 1.5$  eV was carried out for the putative (unstable) AFM phase. One can see in Figs. S1(a)–S1(c) that the calculated FS volume at this  $k$  slice is systematically reduced upon increasing  $U$ .

This shrinkage is also seen in the calculated band dispersion in Figs. S1(d)–S1(f). Importantly, none of AFM calculations satisfactorily reproduces the experimental data while the matching between the experiment and calculation becomes gradually better upon reducing  $U$ . This is reasonable because the reduction of  $U$  makes the system closer to the NM phase. It is remarked that although the matching between the experiment and calculation becomes the best at  $U = 1.5$  eV, the agreement is still poorer than the case of the NM calculation shown in Fig. 2(b) of the main text. Thus, disagreement of the experimental data with the AFM calculation is not due to the incorrect choice of the  $U$  value, but due to the intrinsic absence of magnetic order in the RuO<sub>2</sub> single crystal.

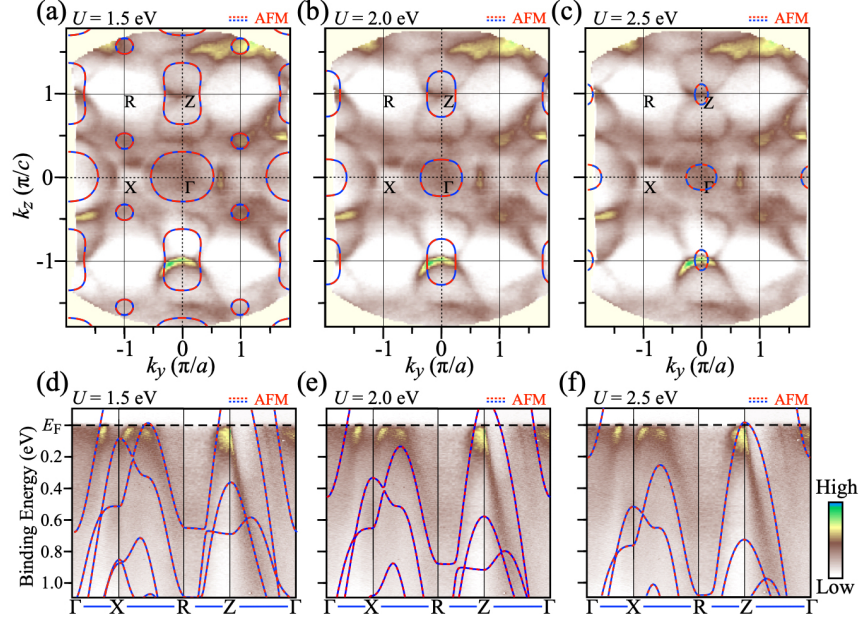


Fig. S 1. **Comparison of Fermi surface between experiment and AFM calculations with different  $U$  values in  $\text{RuO}_2$ .** (a)-(c) FS mapping of  $\text{RuO}_2$  from ARPES at  $T = 40$  K for the (100) surface at  $k_x = 0.0$  obtained with  $h\nu = 110$  eV, overlaid with the calculated FS obtained by the AFM calculation without SOC at  $U = 1.5, 2.0,$  and  $2.5$  eV, respectively. Spin-down and spin-up FSs are indicated by red and blue dashed curves, respectively. (d)-(f) ARPES-intensity mapping for the (100) surface along the  $\Gamma$ XRZ $\Gamma$  cut at  $k_x = 0.0$ , compared with the AFM calculation with  $U = 1.5, 2.0,$  and  $2.5$  eV, respectively. For  $U = 1.5$  eV, the AFM state presented in (a) and (d) actually has a higher energy than the NM state.

## Supplemental Note 2: Surface state at the (100) surface

To clarify the surface or bulk nature of the observed flat band around the  $\Gamma$  point for the (100) surface presented in Figs. 2(d)–2(i), we carried out  $h\nu$ -dependent ARPES measurements. Figure S2(a) shows the  $h\nu$ -dependence of EDC obtained with a normal emission set-up. One can recognize several features dispersing upon  $h\nu$  variation, which originate from the bulk bands. Corresponding to the flat band, a sharp peak is identified in the vicinity of  $E_F$  at  $h\nu = 40$  eV. The energy position of this peak is invariant against the  $h\nu$  variation, supporting its surface nature, while its intensity is strongly modulated by the photoelectron matrix-element effect. These characteristic spectral features are better seen in the ARPES-intensity plot against  $k_x$  and  $E_B$  in Fig. S2(b). Comparison with the calculated bands in the NM phase signifies a reasonable correspondence of dispersive features between the experiment and calculation, such as an electron band bottomed at  $\sim 1.5$  eV at the 4<sup>th</sup>  $\Gamma$  point and a holelike band topped at  $\sim 1.8$  eV at the 5<sup>th</sup>  $\Gamma$  point, confirming its bulk nature. On the other hand, there exist no corresponding bands in the calculation that could account for the peak at  $E_F$ , supporting its surface origin.

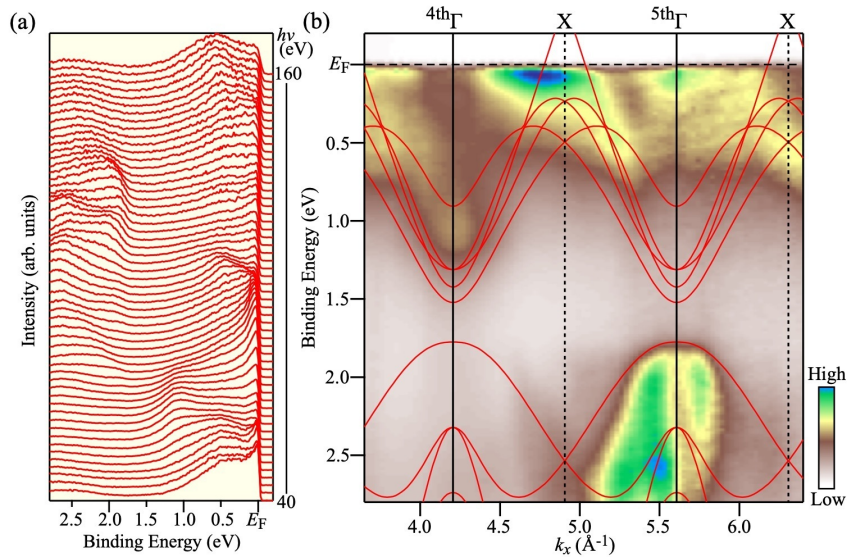


Fig. S 2. **Photon-energy-dependent ARPES data in  $\text{RuO}_2$ .** (a)  $h\nu$  dependence of EDC obtained at the normal-emission setup for the (100) surface of  $\text{RuO}_2$ . (b) Corresponding ARPES intensity in the  $h\nu$  range of 40–160 eV plotted against  $k_x$  and  $E_B$ , together with the calculated band dispersions in the NM phase (red curves) along  $k_x$  axis corresponding to the  $\Gamma X$  cut. We estimated the inner potential to be  $V_0 = 15$  eV from the periodicity of the observed band dispersion.



### Supplemental Note 3: Slab calculations

To clarify the characteristics of the observed SS in more detail, we have carried out surface spectral weight calculations in the NM phase with the Green's function method for the (100), (110), and (101) surfaces by assuming the oxygen-deficient termination because this termination was found to reproduce the experimental results relatively well. One can recognize in the calculation for the (100) surface in Fig. S3(c) the existence of a flat band at  $E_B \sim 0.2$  eV along the  $\Gamma X$  cut. This band is assigned to the SS since it is absent in the bulk-band calculation for the NM phase (black curves), and it would correspond to the flat SS near  $E_F$  observed by ARPES [Figs. 2(d) and S2] (note that the energy location is not the same between the experiment and calculation; this may be improved by tuning the surface lattice parameters and/or the amount of oxygen deficiency). For the (110) surface [Figs. S3(d)-S3(f)], we found similar characteristics, i.e. the existence of a flat SS along the  $\Gamma X$  cut, in line with the ARPES observation of a flat SS in Fig. 3(f). In contrast to the flat SS that commonly appears in both (110) and (100) surfaces, we found that the flat SS does not appear in the (101) surface, as shown in Fig. S3(i). Instead, the spectral weight is widely distributed. We found it rather difficult to obtain a good matching between the experimental and calculated surface band dispersions for the (101) surface. While the reason is unclear at the moment, we speculate that this may be due to the possible lattice deformation of cleaved surface and/or the difference in the amount of oxygen deficiency.

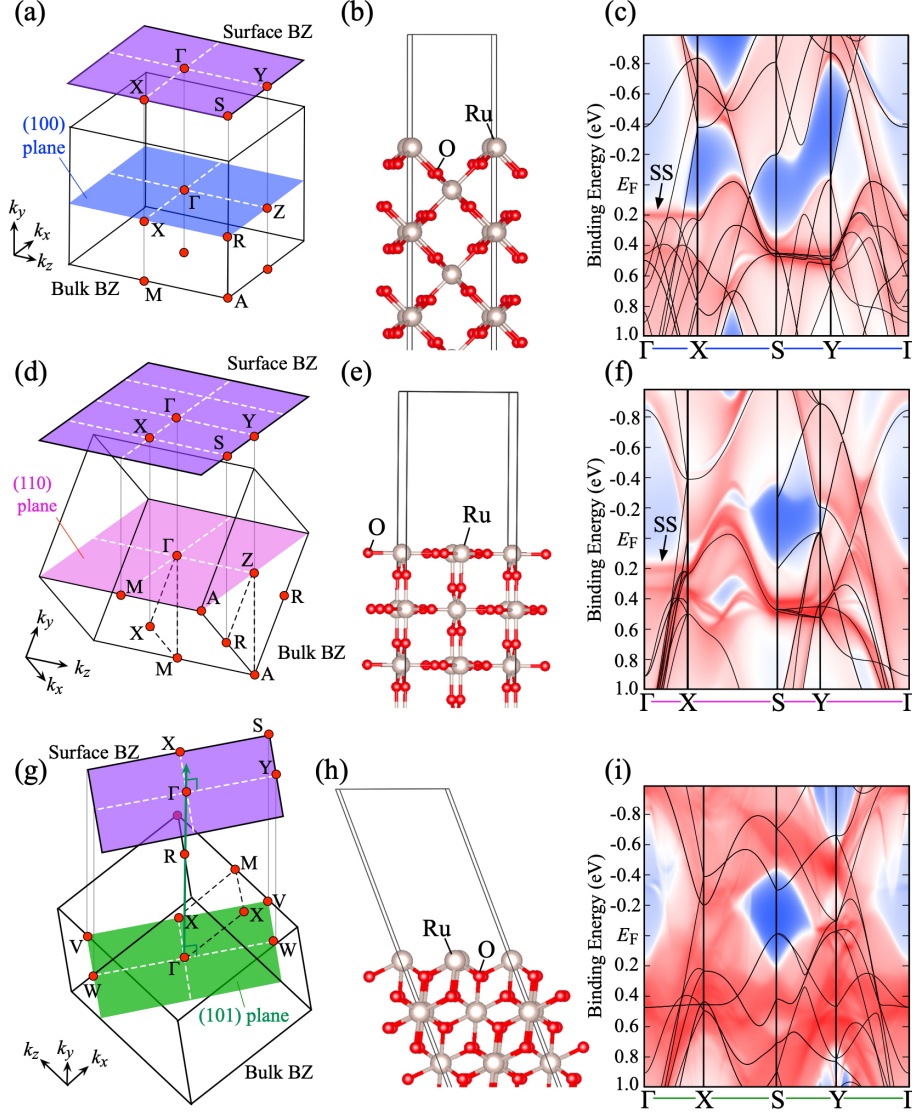


Fig. S 3. **Slab calculations for (100), (110), and (101) orientations in  $\text{RuO}_2$ .** (a) Bulk BZ (blue shade) and corresponding surface BZ (purple shade) projected onto the (100) plane of  $\text{RuO}_2$ . (b) Slab structure for the (100) orientation assumed in the calculation. (c) Corresponding calculated surface spectral weight in the NM phase along the high-symmetry cut projected onto the (100) plane, obtained with the Green's function method. The SOC is included in the calculation. Bulk band calculation (without SOC) along  $k$  cuts that can be projected onto the surface high-symmetry lines is overlaid with black curves. (d)–(f) Same as (a)–(c) but for the (110) surface. (g)–(i) Same as (a)–(c) but for the (101) surface. Flat bands at  $E_B \sim 0.2$  eV along the  $\Gamma X$  cut in (c) and (f) are assigned to the SS since corresponding bands are absent in the bulk band calculation (solid curves), and these bands are actually identified by ARPES at around  $E_F$  in Figs. 2(d), 2(f), 2(h), and 3(d). Flat bands are not clearly seen for the (101) surface in (i); this may account for the ARPES observation that the flat SS are absent only for the (101) surface.

#### Supplemental Note 4: Spin-resolved ARPES data

To reconfirm the absence of altermagnetic band splitting in bulk bands, we have carried out spin-resolved ARPES measurements at CASSIOPÉE beamline in synchrotron SOLEIL. Figures S4(a) and S4(c) show the spin-resolved EDCs at  $T = 40$  K measured at a  $k$  point midway between the  $\Gamma$  and M points for the (100) surface, where the AFM calculation predicts a sizable (more than 0.4 eV) spin splitting. One can immediately recognize no difference between the spin-up and spin-down EDCs along the  $y$ -axis (we set the  $x$  and  $y$  axes parallel to the sample surface at the normal emission with the  $y$ -axis being along [001]). The observed spin polarization is essentially zero within experimental uncertainty as shown in Figs. S4(b) and 4(d). We also found that the polarization along the  $x$ -axis is also zero (not shown). This supports the absence of altermagnetic band splitting at the (100) surface. We have carried out spin-resolved ARPES measurements also for the (110) surface at the  $k$  point where the altermagnetic splitting is theoretically predicted in the AFM calculation, but found no clear spin polarization [Figs. S4(e)–S4(h)].

#### Supplemental Note 5: Influence of SOC to the calculated band structure

To clarify the influence of SOC on the calculated band structure of  $\text{RuO}_2$ , we show in Figs. S5(a) and S5(b) a side-by-side comparison of the calculated band dispersions in the NM phase along the XMARX cut ( $k_x = 1.0$ ) obtained without and with SOC, respectively, overlaid with the corresponding ARPES intensity at the (100) surface. One can see an overall similarity in these calculations, in particular, regarding their  $(E, k)$  position. A closer look reveals a small band doubling in the calculation with SOC, together with a hybridization gap at the intersection in some of these bands, as highlighted by the band crossing point associated with the DNL along the MA cut in Figs. S5(a) and S5(b). This trend is also seen in the calculation for the  $\Gamma$ XRZ $\Gamma$  line ( $k_x = 0.0$ ) shown in Figs. S5(c) and S5(d). The band doubling predicated in the calculation is so small that it is unlikely to be resolved within our experimental accuracy. At the (101) surface, one can see a similar band doubling in the calculations with SOC [Figs. S5(e)–S5(h)], whereas the doubling leads to more complex band dispersions at particular  $k$  cuts like the  $A\Sigma$  cut due to the band hybridization. The calculation with SOC along the  $A\Sigma$  cut shows a relatively good agreement with the ARPES intensity near  $E_F$ , implying a finite influence of SOC on the experimental spectral feature.

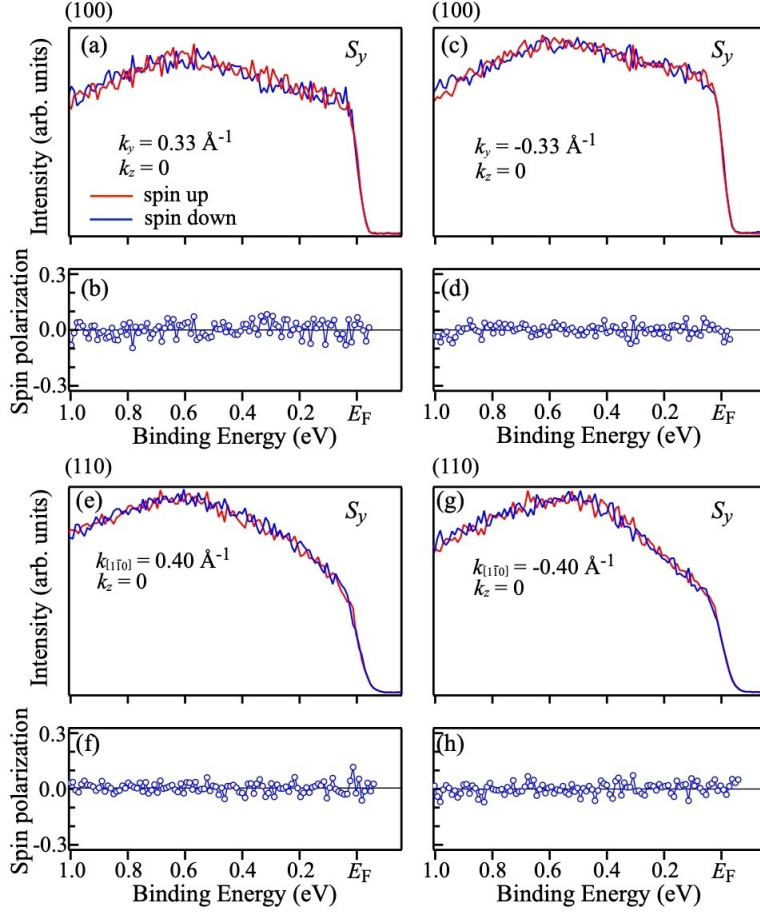


Fig. S 4. **Spin-resolved EDCs and spin polarizations in RuO<sub>2</sub>.** (a)-(d) Spin-resolved EDCs and  $E_B$  dependence of spin polarization at the wave vectors  $k_y = \pm 0.33 \text{ \AA}^{-1}$  along the  $\Delta Y$  cut [see red line in Fig. 2(f) in the main text] at the (100) surface. (e)-(h) Same as (a)-(d) but for the (110) surface, obtained at the wave vectors  $k_{[\bar{1}10]} = \pm 0.40 \text{ \AA}^{-1}$  along the  $\Gamma M$  cut [see red line in Fig. 3(d) in the main text]. There is no spin splitting with the experimental precision, supporting the absence of magnetic order in RuO<sub>2</sub>.

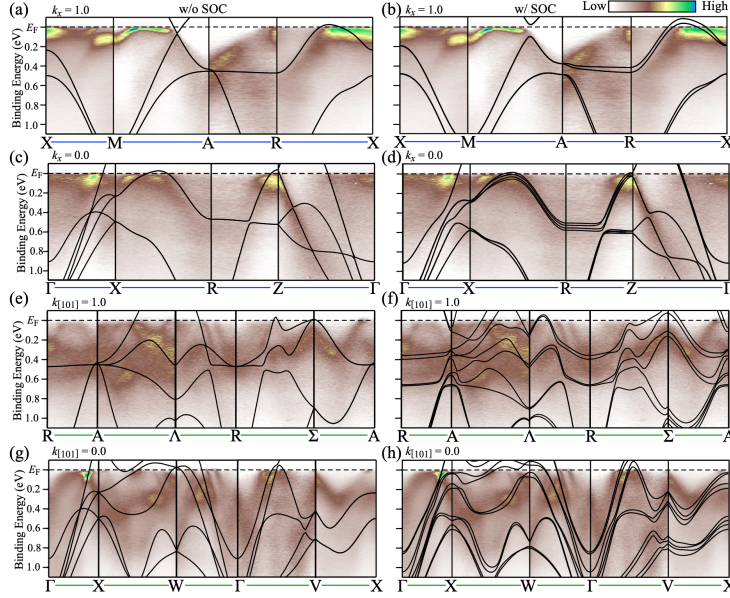


Fig. S 5. **Comparison of band dispersion between experiment and NM calculations with and without SOC.** (a), (b) Calculated band dispersions in the NM phase of RuO<sub>2</sub> without and with SOC, respectively, along the principal  $k$  cut (XMARX cut) at  $k_x = 1.0$  for the (100) surface. ARPES intensity [same as Fig. 2(d) in the main text] is also overlaid. (c), (d) Same as (a) and (b), respectively, but along the  $\Gamma$ XRZ $\Gamma$  cut at  $k_x = 0.0$  for the (100) surface. (e), (f) Same as (a) and (b), respectively, but along the principle  $k$  cut at  $k_{[101]} = 1.0$  for the (101) surface. (g), (h) Same as (e) and (f), respectively, but at  $k_{[101]} = 0.0$  for the (101) surface.